Mechanical Systems and Signal Processing 28 (2012) 638–659

Contents lists available at SciVerse ScienceDirect

Mechanical Systems and Signal Processing

journal homepage: www.elsevier.com/locate/ymssp

A multi-scale pseudo-force model in wavelet domain for identification of damage in structural components

Maosen Cao [a,b], Li Cheng [b], Zhongqing Su [b,*], Hao Xu [b]

[a] Department of Engineering Mechanics, College of Mechanics and Materials, Hohai University, Nanjing 210098, People's Republic of China
[b] Department of Mechanical Engineering, The Hong Kong Polytechnic University, Hung Hom, Kowloon, Hong Kong SAR

ARTICLE INFO

Article history:
Received 13 June 2011
Received in revised form
4 September 2011
Accepted 12 November 2011
Available online 4 January 2012

Keywords:
Multi-scale modeling and identification
Pseudo-force model
Signal processing
Wavelet transform
Damage detection
Dynamic equilibrium

ABSTRACT

Damage identification using wavelet-transform (WT)-processed vibration signals has been practiced over the years. In most studies, WT was used as an effective signal analysis tool to filter out noise and bring damage-incurred singularities into prominence. In spite of its proven effectiveness, such a processing is often carried out without theoretical footstones sustained by solid mechanics models, which are able to link characteristics of WT with features of damage. In the present work, a multi-scale pseudo-force model over wavelet domain was developed for vibration-based damage identification. By canvassing damage-caused local perturbance to dynamic equilibrium characteristics of a structural component, the underlying hypostasis of the model has explicit physical implication, addressing features of damage (e.g., a slot or a fine crack) and enabling a sophisticated solution to multi-scale modeling and identification of damage. In the model, WT was used as a multi-scale differential operator to acquire higher-order derivatives of equation of motion for characterizing damage of tiny dimension. The multi-scale nature brings additional benefits to enhance robustness of the detection under noisy measurement conditions. Without loss of generality, an Euler–Bernoulli beam component (EBC) was considered to facilitate understanding of the principle of the model. As proof-of-concept validation, a fine crack in an EBC was quantified using the model through numerical simulation and experiment. Satisfactory results have demonstrated the effectiveness of the model in evaluating fine damage and enhancing tolerance of the detection to measurement noise.

1. Introduction

Most mechanical, aerospace and civil structures continue their services in spite of progressive ageing and accumulative formation of damage over their lifespan. Damage (e.g., fatigue crack or corrosion) can demolish the integrity of a structure without timely awareness, jeopardizing the safe operation and reliability of the entire system. To address such a concern, various nondestructive evaluation (NDE) techniques have been developed, playing an indispensable role in detecting structural damage in an early stage and subsequently monitoring its further deterioration, whereby failure of the system can be prevented through appropriate remediation. Intensive research and development of NDE over the past two decades have led to a formidable number of techniques available with demonstrated success in various applications [1–5]. Amongst them, much effort has been focused on the global vibration-based methods (using for example eigen-frequencies [6,7], mode shapes [7,8], electro-mechanical impedance [9], frequency response functions [10–12] or damping properties [13]). The basic premise of global vibration-based identification resides on the fact that occurrence of damage induces

---

[*] Corresponding author. Tel.: +852 2766 7818; fax: +852 2365 4703.
E-mail address: MMSU@polyu.edu.hk (Z. Su).

0888-3270/$ - see front matter © 2011 Elsevier Ltd. All rights reserved.
doi:10.1016/j.ymssp.2011.11.011

singularities in structural dynamic characteristics such as mode shapes or impedance, and these singularities are in turn manifested in vibration responses obtained from the structure (e.g., shift in eigen-frequencies or alternation in model shapes). Once vibration responses are captured, proper signal processing tools in the time domain [14], frequency domain [15] or joint time–frequency domain (e.g., short-time Fourier transform, Wigner–Ville distribution and wavelet transform (WT)) [1,15,16] are applied to extract signal features associated with damage, by benchmarking against baseline signals obtained from an intact counterpart, for further damage characterization.

Amongst various signal processing tools for NDE, WT has proven cost-effectiveness in dealing with vibration signals [17–23]. Representatively, Wang and Deng [24] detected a crack in a beam using continuous-wavelet-transform (CWT)-processed structural responses. Zhong and Oyadiji [25] proposed a damage detection approach to protrude damage-incurred abnormalities in first four order mode shapes of a beam-like structure using CWT analysis. Also analyzing CWT-processed mode shapes, Gentile and Messina [26] revealed an open crack in beam structures. Hong et al. [27] employed the Lipschitz exponent estimated by CWT to measure the abrupt changes in the fundamental mode shape so as to characterize damage. In most applications, WT has been used as an effective signal processing tool to filter out signal noise and stand out damage-incurred signal singularity [28–32]. Such a processing, however, is often conducted without a solid backup from explicit mechanics models or theoretical footstones; as a result there is a clear lack of physical correlation between variation in damage and distinction in damage-induced singularities in a vibration signal obtained using WT.

On the other hand, traditional global vibration-based damage detection, when implemented in practice, may suffer from some drawbacks including the following:

(i) strong dependence on benchmark counterparts and baseline signals for comparison (the difference in between indicates the presence of damage) [33];
(ii) necessity of global models to bridge changes in structural responses with damage parameters, and therefore the need of knowledge on boundary conditions beforehand;
(iii) requirement of well-controlled excitations to activate the structural vibration;
(iv) excessive susceptibility to fluctuating operational and measurement conditions, in which measurement noise may remarkably modulate dynamic characteristics of the structure under inspection and blur damage-induced singularity;
(v) insensitivity to damage before it reaches a conspicuous extent (e.g., 10% of the characteristic dimension/area of the structure), because damage is a local event, which would not alter global responses phenomenally [34].

All of the above demerits can fairly narrow the application domain of global vibration-based damage detection in practice.

Bearing in mind the above deficiencies of most global vibration-based damage detection methods relying on WT, a multi-scale pseudo-force model over the wavelet domain was developed in the work. By canvassing damage-incurred local perturbance to dynamic equilibrium characteristics of the structural component under inspection when subjected to a mono-frequency excitation, the model presents explicit physical implication addressing key features of specific damage such as a slot or a fine crack. Differing from a 'global' approach, which explores vibration responses at a level of entire structure, this model examines, 'locally', a structural component point-by-point, able to circumvent the aforementioned problems of conventional vibration-based detection. In the model, WT was not merely used as a signal processing tool, but a multi-scale differential operator to acquire higher-order derivatives of equation of motion. Characterized by these higher-order derivatives, damage of fine dimension can be detected with high precision. As proof-of-concept validation, numerical simulations were carried out, in which a fine crack in a structural beam component was quantified using the developed model. Experimental verification was then conducted using a scanning laser vibrometer.

2. Pseudo-force model

In principle, the philosophy behind the proposed multi-scale pseudo-force model is applicable to any structural components such as a beam, a plate or a shell, due to its nature of local examination, provided that the dynamic characteristics of the structural component under inspection can be locally described. Without loss of generality, an Euler–Bernoulli beam component (EBC) as shadowed in Fig. 1, which can be a part of a complex system comprising various types of structural components, was considered for its simplification, to facilitate understanding of the model development.

Given the EBC is subject to a transverse excitation, its governing equation, in an intact status (free of damage), can be described locally by [35]

$$\frac{\partial^2}{\partial x^2}\left[E(x)I(x)\frac{\partial^2 w(x,t)}{\partial x^2}\right]+\rho(x)A(x)\frac{\partial^2 w(x,t)}{\partial t^2}=f(x,t), \tag{1}$$

where $w(x,t)$ and $f(x,t)$ are the transverse displacement of the EBC and transverse excitation, respectively, at location x and at moment t. $E(x)$, $I(x)$, $A(x)$ and $\rho(x)$ are Young's modulus, moment of inertia, area of the cross-section and material density at location x, respectively. Note that Eq. (1) applies to every single point or fragment of the EBC, serving as therefore a local equilibrium equation and reflecting the local dynamic characteristics of equilibrium between the inertia force of a fragment of the EBC and the internal forces/moments exerted by its adjacent elements. In this sense, even in the absence of any external force, Eq. (1) is still able to describe the forced vibration of a fragment of the EBC (i.e., excitation is exerted by its adjacent elements).

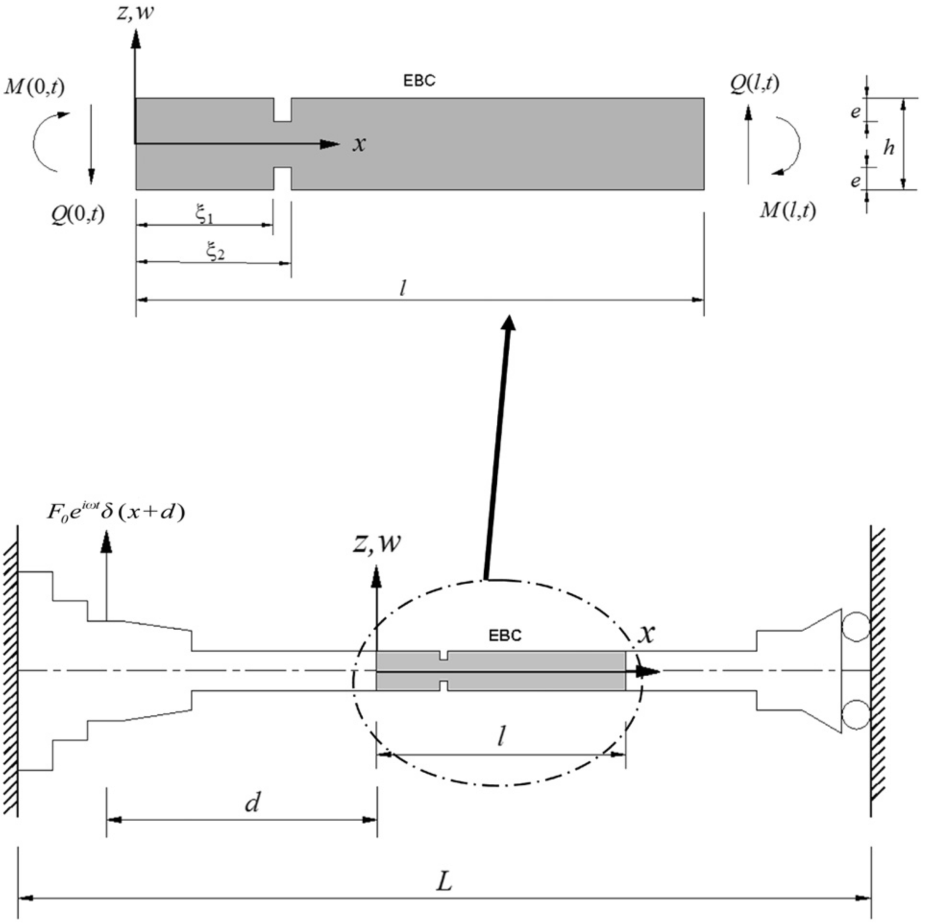

Fig. 1. Structural system containing an EBC with a damaged zone (inset: zoomed-in part containing the EBC).

Consider that the EBC bears a damaged zone symmetric with regard to the beam neutral axis, as seen in Fig. 1. Because Eq. (1) describes the dynamic characteristics of the EBC locally, there are no particular restraints on the boundaries of the EBC and its neighboring components (i.e., independent of boundary conditions and rest of the entire system). The above EBC with a damaged zone can further be depicted using a mechanics model shown in Fig. 2(a), with Fig. 2(b) showing a differential element arbitrarily selected and isolated from the intact region of the EBC. The boundary restrictions of this isolated element exerted by its neighboring components include bending moments ($M(x,t)$ and $M(x,t)+(\partial M(x,t)/\partial x)\mathrm{d}x$ at left and right boundaries, respectively) and shear forces ($Q(x,t)$ and $Q(x,t)+(\partial Q(x,t)/\partial x)\mathrm{d}x$ at left and right boundaries, respectively).

2.1. Pseudo-force model for EBC bearing a slot

Without losing generality, first consider the case that the damaged zone is a slot and the EBC has a uniform rectangular cross-section ($I(x)=I_0$ and $A(x)=A_0$) and even elastic properties ($E(x)=E_0$ and $\rho(x)=\rho_0$). Define the EBC by dividing it into three segments: a damaged segment containing the slot, and two intact segments. In the damaged segment ($\xi_1 \le x \le \xi_2$, where ξ_1 and ξ_2 are the locations of the left and right boundaries of the slot in the coordinate system shown in Fig. 1), the slot causes reductions in both the cross-sectional stiffness and mass. Eq. (1) can thus be rewritten, if there is no external force $f(x,t)$ directly applied within the EBC, as

$$\frac{\partial^2}{\partial x^2}\left\{E_0I_0\left[1-r_1\Pi_{\xi_1,\xi_2}(x)\right]\frac{\partial^2 w(x,t)}{\partial x^2}\right\}+\rho_0A_0\left[1-r_2\Pi_{\xi_1,\xi_2}(x)\right]\frac{\partial^2 w(x,t)}{\partial t^2}=0, \tag{2}$$

where

$$\Pi_{\xi_1,\xi_2}(x)=\begin{cases}0, & x<\xi_1, x>\xi_2 \text{ (for two intact segments)}\\ 1. & \xi_1\le x\le\xi_2 \quad \text{(for damaged segment)}\end{cases}$$

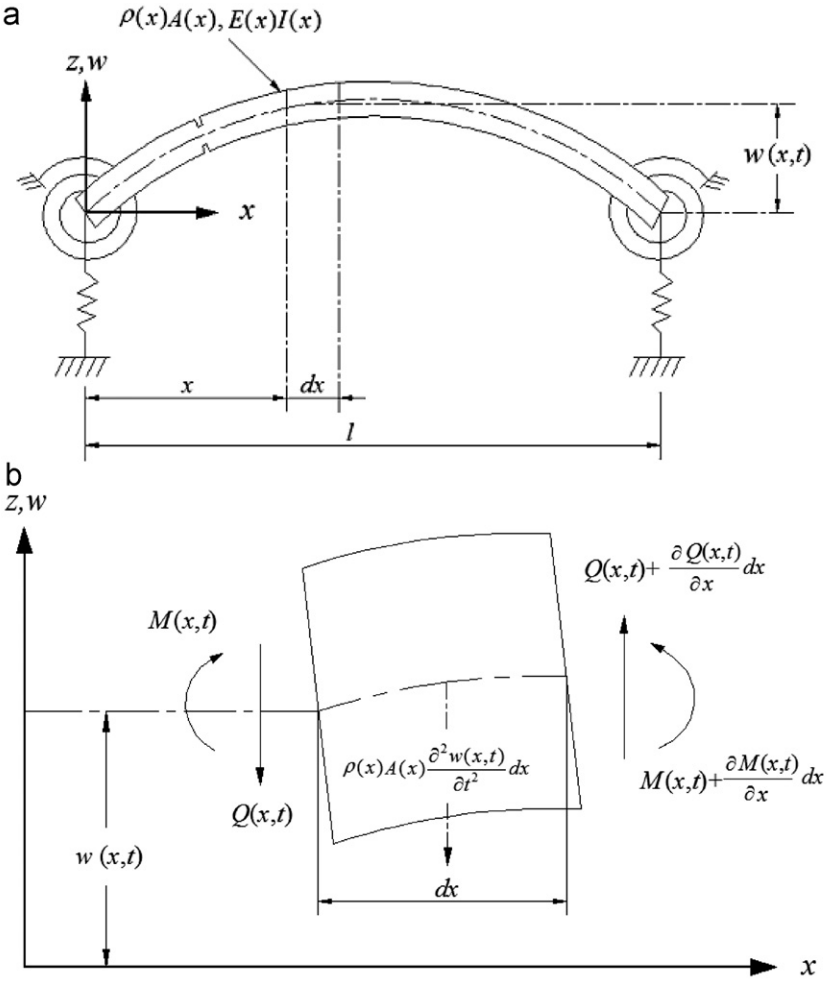

Fig. 2. (a) Mechanics model for an EBC with damage; (b) a differential element isolated from the intact region of the EBC in (a).

In the above, subscript '0' labels those parameters for two intact segments. A boxcar function, Π, differentiates the equation for three segments. $r_1=1-(1-2e/h)^3$ and $r_2=2e/h$ are associated with the slot-caused reductions in flexural stiffness and mass, respectively (h being the height of the intact segment and e being the depth of the slot at each side, as indicated in Fig. 1).

Assuming that a harmonic transverse excitation, $F_0e^{i\omega t}\delta(x+d)$, is applied d away from the left end of the EBC as indicated in Fig. 1 (where F_0 and ω are the magnitude and angular frequency of the excitation, respectively; $\delta(x)$ is a Dirac function; note that ω is not necessarily to be one of the resonant frequencies of the structure), solutions to Eq. (2), describing the transverse motion of the EBC, can be expressed as

$$w(x,t)=W(x)e^{i\omega t}, \tag{3}$$

where $W(x)$ denotes the transverse displacement magnitude of the EBC along the beam.

Substituting Eq. (3) into (2) yields

$$\frac{\mathrm{d}^2}{\mathrm{d}x^2}\left\{E_0I_0\left[1-r_1\Pi_{\xi_1,\xi_2}(x)\right]\frac{\mathrm{d}^2W(x)}{\mathrm{d}x^2}\right\}-\rho_0A_0\left[1-r_1\Pi_{\xi_1,\xi_2}(x)\right]\omega^2W(x)=0, \tag{4}$$

which can further be rewritten as

$$E_0I_0\frac{\mathrm{d}^4W(x)}{\mathrm{d}x^4}-\rho_0A_0\omega^2W(x)=\left[r_1E_0I_0\frac{\mathrm{d}^4W(x)}{\mathrm{d}x^4}-r_2\rho_0A_0\omega^2W(x)\right]\Pi_{\xi_1,\xi_2}(x). \tag{5}$$

The two left-hand-side terms, $E_0I_0(\mathrm{d}^4W(x)/\mathrm{d}x^4)$ and $\rho_0A_0\omega^2W(x)$, are the elastic force (*EF*) and inertia force (*IF*) at location x, respectively. The equation, describing an EBC containing a slot, can be condensed as

$$E_0I_0\frac{\mathrm{d}^4W(x)}{\mathrm{d}x^4}-\rho_0A_0\omega^2W(x)=\mathfrak{R}_{slot}(x)=\pi_{slot}(x)-\Gamma_{slot}(x), \tag{6a}$$

where

$$\pi_{slot}(x)=r_1E_0I_0\frac{d^4W(x)}{dx^4}\Pi_{\xi_1,\xi_2}(x)\text{ and }\Gamma_{slot}(x)=r_2\rho_0A_0\omega^2W(x)\Pi_{\xi_1,\xi_2}(x). \tag{6b}$$

The right-hand side of Eq. (6a) implies that the transverse vibration of an EBC bearing a slot-like damaged zone is equivalent to that of its corresponding intact counterpart subjected to a pseudo-force, denoted by $\Re_{slot}(x)$, which distributes over $[\xi_1, \xi_2]$. Further, as indicated by Eq. (6b), this pseudo-force comprises two components: pseudo-elastic force (*PEF*), $\pi_{slot}(x)$, and pseudo-inertia force (*PIF*), $\Gamma_{slot}(x)$. When the slot depth e in both r_1 and r_2 equals zero (no any damage in the EBC), this pseudo-force vanishes, and Eq. (6a) becomes the equation of motion for an intact EBC. Eqs. (5) and (6) constitute the footstone of a pseudo-force model for depicting an EBC containing a slot. In particular, Eq. (6), linking slot depth e to the pseudo-force, can be inversely used to characterize the slot.

For validation, a slotted EBC with free–free boundary conditions, was simulated using the pseudo-force model defined by Eq. (5). The third-order mode shape of the EBC was substituted into the left-hand-side terms of Eq. (6a); the two terms *EF* and *IF*, as well as their residual (i.e., the value of the left-hand side of Eq. (6a)), are diagramed in Fig. 3(a). In parallel and independently, the same mode shape was substituted into the right-hand-side terms of Eq. (6a); the two terms *PEF* ($\pi_{slot}(x)$) and *PIF* ($\Gamma_{slot}(x)$), as well as their residual (i.e., the value of the right-hand side of Eq. (6a)) are diagramed in Fig. 3(b). Two residuals are then combined in Fig. 3(c) for comparison, in which the perfect match between the left-hand and right-hand sides of Eq. (6a) has demonstrated the correctness of the proposed pseudo-force model.

2.2. Pseudo-force model for EBC bearing a crack

Extending the above discussion to an extreme case when $\xi_1\approx\xi_2$, the slot is degraded to a crack with ignorable span along the beam axis. The boxcar function in Eq. (2) can thus be squeezed to a Dirac function $\delta(x)$ at $\xi=(\xi_1+\xi_2)/2$, leading to a revamped form of Eq. (5) for an EBC bearing a crack:

$$E_0I_0\frac{d^4W(x)}{dx^4}-\rho_0A_0\omega^2W(x)=\left[r_1E_0I_0\frac{d^4W(x)}{dx^4}-r_2\rho_0A_0\omega^2W(x)\right]\delta(x-\xi). \tag{7}$$

In light of the properties of Dirac function that $W(x)\,\delta(x-\xi)=W(\xi)\,\delta(x-\xi)$, it yields

$$E_0I_0\frac{d^4W(x)}{dx^4}-\rho_0A_0\omega^2W(x)=\left[r_1E_0I_0\left.\frac{d^4W(x)}{dx^4}\right|_{x=\xi}-r_2\rho_0A_0\omega^2W(\xi)\right]\delta(x-\xi). \tag{8}$$

Similar to the operation in the above for deriving Eq. (6), one has

$$E_0I_0\frac{d^4W(x)}{dx^4}-\rho_0A_0\omega^2W(x)=\Re_{crack}(x)=\pi_{crack}(x)-\Gamma_{crack}(x). \tag{9}$$

The right-hand-side term of Eq. (9) alludes to that the transverse vibration of an EBC containing a crack can be depicted by the transverse vibration of its corresponding intact counterpart subjected to a pseudo-force at $\xi=(\xi_1+\xi_2)/2$; the pseudo-force, denoted by $\Re_{crack}(x)$, is defined as

$$\Re_{crack}(x)=\pi_{crack}(x)-\Gamma_{crack}(x). \tag{10a}$$

This pseudo-force includes two components:

$$\pi_{crack}(x)=r_1E_0I_0\left.\frac{d^4W(x)}{dx^4}\right|_{x=\xi}\delta(x-\xi)\text{ and }\Gamma_{crack}(x)=r_2\rho_0A_0\omega^2W(\xi)\delta(x-\xi), \tag{10b}$$

corresponding to the crack-caused *PEF* and *PIF*, respectively. Further letting $K=r_1E_0I_0(d^4W(x)/dx^4)|_{x=\xi}-r_2\rho_0A_0\omega^2W(\xi)$, a compact form of the pseudo-force model for a cracked EBC can be given as

$$E_0I_0\frac{d^4W(x)}{dx^4}-\rho_0A_0\omega^2W(x)=K\delta(x-\xi), \tag{11}$$

where K and ξ are associated with the severity and location of the crack, respectively. Eqs. (8)–(11) serve as the rationale of a pseudo-force model for an EBC bearing a crack, which can be used to quantify the crack.

3. Crack identification using pseudo-force model

The pseudo-force models described by Eqs. (6) and (11) established the basic framework for quantitatively identifying slots and cracks in an EBC, respectively. In what follows, identification of a fine crack in an EBC using the developed model is detailed.

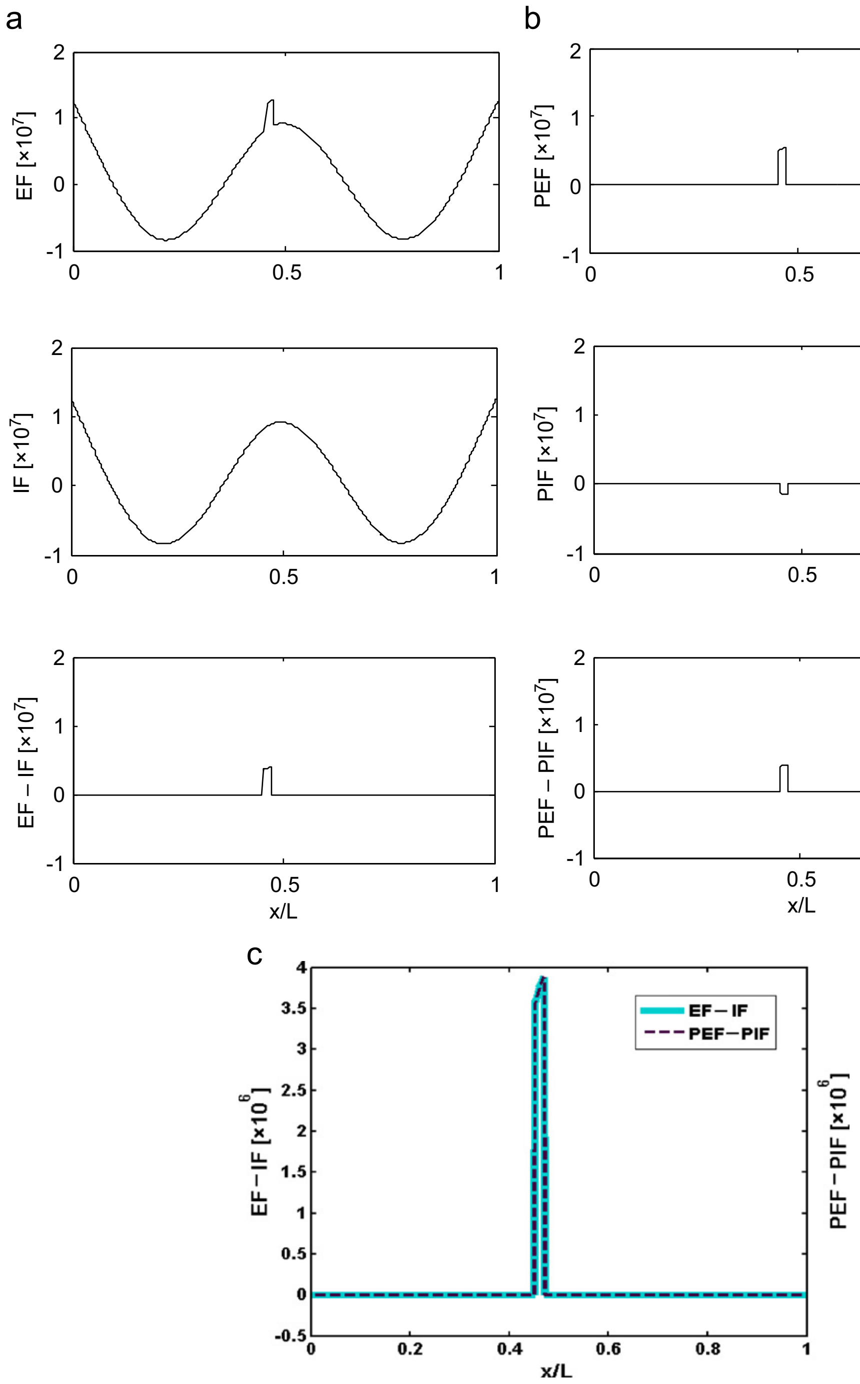

Fig. 3. Validation of the developed pseudo-force model: (a) terms *EF*, *IF* and *EF–IF* of Eq. (6a); (b) terms *PEF*, *PIF* and *PEF–PIF* of Eq. (6a); (c) comparison between left-hand-side (*EF–IF*) and right-hand-side (*PEF–PIF*) terms of Eq. (6a).

3.1. Principle

For a given EBC, once the transverse displacement magnitude $W(x)$ is obtained across the beam span and substituted to the left-hand side of Eq. (11), a residual (i.e., the pseudo-force $\Re_{crack}(x) = K\delta(x-\xi)$) becomes prominent at the location of the crack, if any, compared with other intact regions. This can be regarded as a local perturbance generated by the damage to the dynamic characteristics of the EBC. Such a damage-induced residual is reflected by a drastic change described by the Dirac function, $\delta(x-\xi)$, in Eq. (11). That is because, as revealed by the model, the crack is the only contributor responsible for the generation of the pseudo-forces. The location at which the Dirac function stands out drastically suggests the position of the crack, while the magnitude of the change, scaled by K, can further be used to evaluate the severity of the crack.

Residing on such a mechanics model, the damage detection algorithm based on the developed pseudo-force model exhibits explicit physical implication addressing damage characteristics, thus possessing unique features compared to traditional global vibration-based damage detection techniques in the following aspects:

(i) characterized by the fourth-order differential equation of motion ($\mathrm{d}^4W(x)/\mathrm{d}x^4$, as seen in Eq. (11)), it is anticipated that detection capability can be improved significantly in comparison with those based on displacement $W(x)$ or its lower-order derivatives;
(ii) the model canvasses a structural component point-by-point at a local level without using a global model, and it is therefore independent of the rest of the system beyond the inspection region. Without relying on any global model, such a approach can be extended to other types of structural components provided that their local dynamic equilibrium relationship is known *a priori*;
(iii) thanks to the local character of the model, knowledge on overall structural boundary conditions is not required beforehand;
(iv) by the same token, the baseline information collected from an intact structure is not required. As long as the pseudo-forces are detected, damage is anticipated to be present, whose location and severity can be estimated in light of the Dirac function in Eq. (11);
(v) owing to the fact that a global model or a benchmark is not mandatory, influences of varying environmental factors (e.g., temperature and humidity fluctuation) on structural dynamic properties are naturally avoided;
(vi) the algorithm is expected to outperform traditional vibration-based detection in characterizing damage of small size such as a fine crack. That is because traditional approaches are based on the changes in global structural properties, which would however not be pronounced until the damage reaches a conspicuous extent; whereas the pseudo-force model is not limited by the damage size in principle because any damage regardless of its size creates local perturbance to the structural dynamic characteristics, generating pseudo-forces;
(vii) as long as the structural component undergoes steady vibration (e.g., under the normal operation of the system), no additional excitation source is required, which provides certain flexibility for practical implementation of this algorithm;
(viii) the algorithm is essentially underpinned by a mechanics model, rendering explicit mechanics and physical justification for conducting damage identification.

3.2. Limitation of the model

In spite of the appealing features enumerated in the above, it is anticipated that the proposed pseudo-force model can be susceptible to measurement noise, due to the fourth-order derivatives term $\mathrm{d}^4W(x)/\mathrm{d}x^4$ in Eq. (11). The reason can be explained as follows. Letting $\overline{\mathbf{F}}(f)$ be the Fourier counterpart of $W(x)$, the nth-order derivative of $W(x)$ is expressed as [36]

$$\frac{\mathrm{d}^n W(x)}{\mathrm{d}x^n} \leftrightarrow (-i2\pi f)^n \overline{\mathbf{F}}(f), \tag{12}$$

where notation '↔' stands for *equivalence*. It is understandable that the measurement noise is distributed randomly in a broad frequency range and more dominantly at higher frequencies. As a result, operation of '$(-i2\pi f)^n$' by Eq. (12) magnifies the noise components to a considerable level. By way of illustration, Fig. 4(a) shows $W(x)$ of an EBC containing a crack (see Damage Scenario I in Table 1) obtained in simulation, to which a white noise with a signal-to-noise ratio (*SNR*) of 100 was added; Fig. 4(b) presents the fourth-order derivative of the noise-corrupted $W(x)$, $\mathrm{d}^4W(x)/\mathrm{d}x^4$, to observe the noise components become dominant after the differentiation, masking any damage-induced singularity. This example iterates a common problematic issue in vibration-based damage detection involving higher-order derivatives. To tackle this problem, one can use a lower sampling rate to acquire $W(x)$, but this is at the expense of sacrificing sufficient information to describe damage. Although some theoretical justifications are available to help select an optimal sampling rate [37], it is still case-dependent in practical applications, due to the difficulty in estimating the noise level aforehand. Such a limitation fairly impairs the applicability and effectiveness of the proposed model, calling for tactic to mitigate noise influence.

4. Enhanced pseudo-force model using multi-scale wavelet transform

To tackle the noise interference in high-order derivatives, the pseudo-force model in space domain, defined by Eq. (11), was retrofitted in a WT domain (space-scale domain) using Gaussian WT.

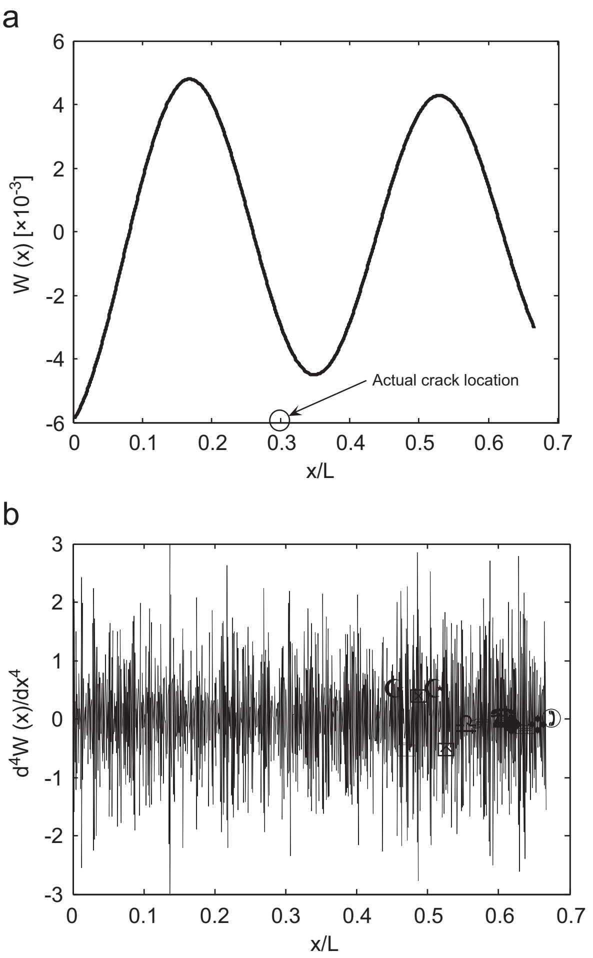

Fig. 4. (a) $W(x)$ of an EBC containing a crack (Damage Scenario I in Table 1); (b) its corresponding 4th-order derivative ($d^4W(x)/dx^4$).

Table 1
Damage scenarios used in simulation ($\xi=0.3$ m).

Damage scenario	**Crack severity** (β)	**Excitation frequency** (ω (Hz))	**Modal frequency before** ω (ω_i (Hz))	**Modal frequency after** ω (ω_j (Hz))	***SNR***
I	0.1	2105.86	$\omega_5=1787.55$	$\omega_6=2596.56$	100
II	0.1	1453.05	$\omega_4=1134.74$	$\omega_5=1787.55$	∞
III	0.1	1453.05	$\omega_4=1134.74$	$\omega_5=1787.55$	85
VI	0.1	2105.86	$\omega_5=1787.55$	$\omega_6=2596.56$	70
V	0.2	2914.85	$\omega_6=2596.54$	$\omega_7=3560.18$	65
VI	0.2	2914.85	$\omega_6=2596.54$	$\omega_7=3560.18$	55
VII	0.3	5080.57	$\omega_8=4682.68$	$\omega_9=5950.99$	60
VIII	0.3	5080.57	$\omega_8=4682.68$	$\omega_9=5950.99$	50

4.1. Gaussian WT

The transverse displacement magnitude, $W(x)$, in space-domain can be transformed into space-scale domain (*scale* is inversely proportional to frequency) via CWT [36], in accordance with

$$\mathcal{W}_{\psi}^{W}(s,u)=\langle W,\psi\rangle=\frac{1}{\sqrt{s}}\int_{-\infty}^{+\infty}W(x)\psi\left(\frac{x-u}{s}\right)dx, \tag{13}$$

where $\mathcal{W}_{\psi}^{W}(s,u)$ is the CWT coefficient of $W(x)$ in space-scale domain (denoted by W for short in following CWT and differentiation equations) with respect to wavelet $\psi(x)$ (ψ for short); s and u are the *scale* (or *dilation*) and *space* (or *translation*) parameters, respectively. $\mathcal{W}_{\psi}^{W}(s,u)$ reflects a measure of the similarity between $W(x)$ and $\psi(x)$. Computationally,

$\mathcal{W}_{\psi}^{W}(s,u)$ can be achieved using manipulation of convolution product:

$$\mathcal{W}_{\psi}^{W}(s,u) = W*\overline{\psi} = \frac{1}{\sqrt{s}}\int_{-\infty}^{+\infty} W(x)\overline{\psi}\left(\frac{x-u}{s}\right)\mathrm{d}x, \tag{14}$$

where $\overline{\psi}(x) = \psi(-x)$ and the asterisk denotes *convolution*. According to Eq. (14), it can be seen that $\mathcal{W}_{\psi}^{W}(s,u)$ actually calibrates the degree of correlation between $W(x)$ and a scaled and shifted $\overline{\psi}(x)$.

To ensure that the inverse transform of CWT is tenable, $\psi(x)$ has to satisfy the admissibility condition [36]:

$$\int_{-\infty}^{+\infty} \frac{|\hat{\psi}(\omega)|^2}{|\omega|}\mathrm{d}\omega < \infty, \tag{15}$$

where $\hat{\psi}(\omega)$ is the Fourier counterpart of $\psi(x)$. In addition, energy of $\psi(x)$ is normalized in this study according to

$$\int_{-\infty}^{+\infty} \psi^2(x)\mathrm{d}x = 1. \tag{16}$$

The above-briefed CWT analysis was then employed to revamp the developed pseudo-force model, so as to enhance its capacity of noise-tolerance during the procedure to obtain $\mathrm{d}^4W(x)/\mathrm{d}x^4$. In the study, the Gaussian wavelet family was adopted as mother wavelet $\psi(x)$, because this series of wavelets provides merits including smoothness, differentiability, localization in space-scale domain, explicit mathematical expressions and flexibility in manipulation. Mathematically, the Gaussian wavelet family originates from the classical Gaussian function whose energy-normalized form is

$$g^0(x) = \frac{1}{\sqrt[4]{2/\pi}}e^{-x^2}, \tag{17}$$

where $g^0(x)$ is the classical Gaussian function. Based on Eq. (17), the Gaussian wavelet family can be expressed in a general form as

$$g^p(x) = C_p(-1)^p\frac{\mathrm{d}^p g^0(x)}{\mathrm{d}x^p}, \tag{18}$$

where C_p is a constant such that $g^p(x)$ satisfies Eq. (16), and integer p specifies the number of vanishing moments or approximation order. If a wavelet has p vanishing moments, then the approximation order of the transform is also p, and the wavelet is referred to as the pth-order wavelet. The sub-wavelets at scale s can further be derived using $g^0(x)$ as

$$g_s^p(x) = C_p(-1)^p s^p\frac{\mathrm{d}g_s^0(x)}{\mathrm{d}x^p}, \tag{19}$$

in which $g_s^0(x) = (1/\sqrt{s})g^0(x/s)$. The first six order Gaussian wavelets, $g^p(x)$ $(p = 1,2,\ldots,6)$, which have often been used as the wavelets in a variety of damage identification practices [26,30,38], are formulated in Table 2 in terms of Eq. (18). In particular, the 1st-order ($g^1(x)$) and 5th-order ($g^5(x)$), to be used in the following, are shown in Fig. 5. Applying a selected wavelet $g^p(x)$ to process captured $W(x)$, the CWT coefficient, $\mathcal{W}_{g^p}^{W}(s,u)$, becomes, according to Eq. (14)

$$\mathcal{W}_{g^p}^{W}(s,u) = W*\overline{g}^p = \frac{1}{\sqrt{s}}\int_{-\infty}^{+\infty} W(x)\overline{g}^p\left(\frac{x-u}{s}\right)\mathrm{d}x, \tag{20}$$

where $\overline{g}^p(x) = g^p(-x)$. $\mathcal{W}_{g^p}^{W}(s,u)$ is the CWT coefficient of $W(x)$ over wavelet domain obtained using wavelet $g^p(x)$.

4.2. Gaussian wavelet for differential transform

In accordance with Eqs. (19) and (20), as well as the theorem of convolution differentiation

$$\frac{\mathrm{d}}{\mathrm{d}u}(W*g^p)(u) = \frac{\mathrm{d}W}{\mathrm{d}x}*g^p(u) = W*\frac{\mathrm{d}g^p}{\mathrm{d}x}(u), \tag{21}$$

Table 2
Mathematic description of the first six order Gaussian wavelets.

$g^p(x) = C_pD_pg^0(x)$, $(g^0(x) = (2/\pi)^{-1/4}e^{-x^2})$		
	C_p	D_p
$g^1(x)$	1	$-2x$
$g^2(x)$	$1/\sqrt{3}$	$-2+4x^2$
$g^3(x)$	$1/\sqrt{15}$	$12x-8x^3$
$g^4(x)$	$1/\sqrt{105}$	$12-48x^2+16x^4$
$g^5(x)$	$1/(3\sqrt{105})$	$-120x+160x^3-32x^5$
$g^6(x)$	$1/(3\sqrt{1155})$	$-120+720x^2-480x^4+64x^6$

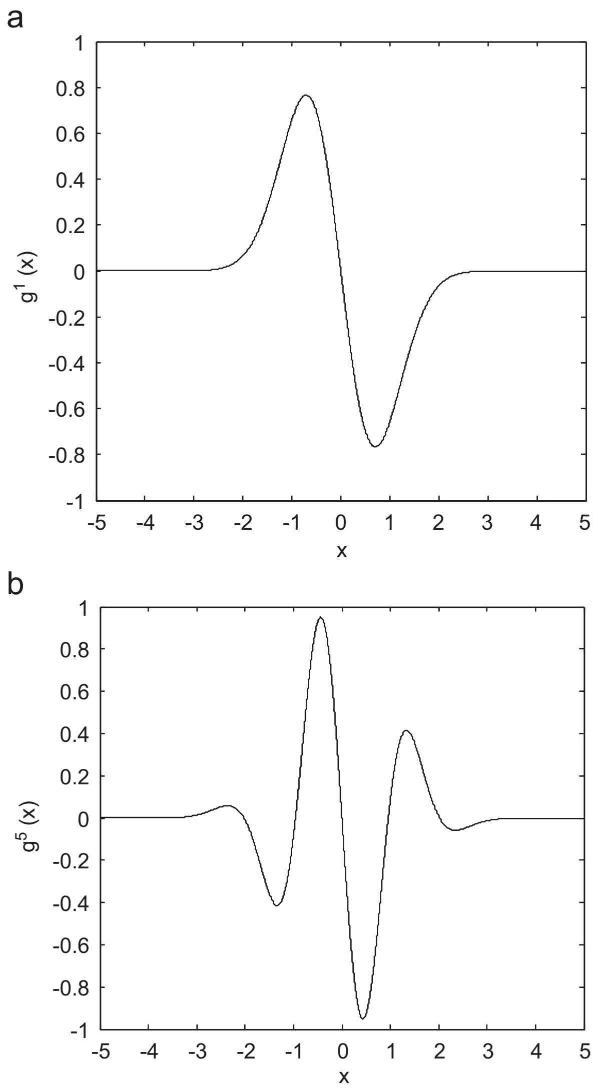

Fig. 5. Gaussian wavelets used in the model: (a) $g^1(x)$; (b) $g^5(x)$.

where the qth-order derivative of $W(x)$ can be obtained in virtue of the pth-order Gaussian wavelet as

$$\frac{d^q W}{dx^q} * \bar{g}_s^p(u) = W * \frac{d^q \bar{g}_s^p}{dx^q}(u) = \frac{C_p(-1)^p s^p}{C_{p+q}(-1)^{p+q} s^{p+q}} W * \bar{g}_s^{p+q}(u). \tag{22}$$

Eq. (22) renders a Gaussian wavelet-based differential transform, to achieve higher-order differentiation involved in the pseudo-force model in Eq. (11). It tactically acquires high-order derivatives of $W(x)$ by differentiating $g^p(x)$ instead of $W(x)$ itself. Therefore, the magnification of measurement noise contained in $W(x)$ during the procedure of differentiation can be circumvented. Such a trait is crucial to the mitigation of influence of measurement noise and uncertainties on $d^4W(x)/dx^4$, ushering an avenue to enhance the practicability and accuracy of the damage detection algorithm based on the developed pseudo-force model.

4.3. *Enhanced model: multi-scale pseudo-force model*

Taking advantage of the noise immunity of high-order derivatives of $W(x)$ obtained via Gaussian wavelet, the pseudo-force model, developed in one-dimensional space domain and described by Eq. (11), was retrofitted in wavelet domain using $g^1(x)$, as

$$E_0 I_0 \frac{d^4 W}{dW^4} * \bar{g}_s^1(u) - \rho_0 A_0 \omega^2 W * \bar{g}_s^1(u) = K\delta_\xi * \bar{g}_s^1(u). \tag{23}$$

In the above, $\overline{g}_s^1 * \delta_\xi(u)$ is the convolution between $\overline{g}_s^1(x)$ and $\delta(x-\xi)$ where $\delta_\xi(x) = \delta(x-\xi)$ (hereinafter δ_ξ standing for $\delta_\xi(x)$). Applied with the Gaussian wavelet-based differential transform defined by Eq. (22), $(\mathrm{d}^4W/\mathrm{d}x^4) * \overline{g}_s^1(u)$ in the first left-hand-side term of Eq. (23) becomes

$$\frac{\mathrm{d}^4W}{\mathrm{d}x^4} * \overline{g}_s^1(u) = W * \frac{\mathrm{d}^4\overline{g}_s^1}{\mathrm{d}x^4}(u) = \frac{C_1(-1)^1 s^1}{C_5(-1)^5 s^5} W * \overline{g}_s^5(u) = \frac{1}{C_5 s^4} W * \overline{g}_s^5(u), \tag{24}$$

where C_1 and C_5 are given in Table 2. Substituting Eq. (24) into (23) gives

$$\frac{1}{C_5 s^4} E_0 I_0 W * \overline{g}_s^5(u) - \rho_0 A_0 \omega^2 W * \overline{g}_s^1(u) = K\delta_\xi * \overline{g}_s^1(u). \tag{25}$$

Furthermore, capitalizing on the property of Gaussian wavelet, $\overline{g}_s^1(x) = g_s^1(-x) = -g_s^1(x)$, and that of Dirac function, $f * \delta_\xi(u) = f(u-\xi)$, one has

$$\frac{1}{C_5 s^4} E_0 I_0 W * \overline{g}_s^5(u) - \rho_0 A_0 \omega^2 W * \overline{g}_s^1(u) = -K g_s^1(u-\xi). \tag{26}$$

Rearranging Eq. (26) yields

$$E_0 I_0 W * \overline{g}_s^5(u) - C_5 s^4 \rho_0 A_0 \omega^2 W * \overline{g}_s^1(u) = -C_5 s^4 K g_s^1(u-\xi). \tag{27}$$

Eq. (27) defines an enhanced two-dimensional pseudo-force model over wavelet (space-scale) domain, derived from the original one-dimensional model (Eq. (11)).

Apart from the enhanced capacity of noise-immunity, another appealing feature of this enhanced model is its multi-scale nature. Kept at a given space while shifted along the scale axis over the space-scale domain, Eq. (27) represents a series of pseudo-force models at various scales (s). This series of models is collectively called *multi-scale pseudo-force model* in the work. For the convenience of presentation, the following notations were introduced:

$$\begin{cases} MEF = E_0 I_0 W * \overline{g}_s^5(u) \\ MIF = C_5 s^4 \rho_0 A_0 \omega^2 W * \overline{g}_s^1(u) \\ MPF = -C_5 s^4 K g_s^1(u-\xi), \end{cases} \tag{28}$$

to simplify Eq. (27) as

$$MEF - MIF = MPF. \tag{29}$$

Eq. (29) explicitly and concisely highlights that existence of any damage in EBC induces a multi-scale pseudo-force (*MPF*, the right-hand-side term) and such a pseudo-force comprises two components: multi-scale elastic force (*MEF*) and multi-scale inertia force (*MIF*). Once a crack is present, *MPF* induces prominent changes in signal features at the location where the crack exists, and the change has the pattern of $-C_5 s^4 K$-scaled $g_s^1(u-\xi)$ centered at $u=\xi$.

Fig. 6 exemplarily shows the results obtained using the *multi-scale pseudo-force model* for an EBC containing a crack (see Damage Scenario II in Table 1) from simulation: *MEF* (containing $\overline{g}_s^5(u)$) is displayed in Fig. 6(a), *MIF* (containing $\overline{g}_s^1(u)$) in (b) and their difference (*viz.*, *MPF*) in (c). To facilitate a better view of the results, contour map of Fig. 6(c) is further represented in Fig. 6(d), to observe a number of zero-crossing lines (i.e., the intersecting lines between the *MPF* surface and $s-(x/L)$ plane at $MPF=0$). In Fig. 6(c) and (d), the central zero-crossing line is able to pinpoint location of the crack, because *MPF* in these figures is featured with pattern of $-C_5 s^4 K$-scaled $g_s^1(u-\xi)$ centered at $u=\xi$, as indicated by Eq. (28). It is noteworthy that, due to the nature of linear transform of CWT, the properties of the original pseudo-force model in space domain are preserved in the enhanced model over space-scale domain, and therefore the enhanced model inherits all those merits of the pseudo-force model enumerated in Section 3.1.

5. Proof-of-concept validation using simulation

As proof-of-concept validation, the enhanced multi-scale pseudo-force model was employed to identify a crack in an EBC using finite element (FE) simulation.

5.1. Case description and modeling

A simply supported steel structure (E_0=206 GPa; ρ_0=7800 kg/m^3) featuring irregular geometry and containing an EBC was considered, as shown schematically in Fig. 7. The EBC is 0.67 m long (l=0.67 m), 0.03 m wide (b=0.03 m) and 0.03 m deep (h=0.03 m). A double-edged fine crack was assumed in the EBC, 0.3 m (ξ=0.3 m) away from the left end of the EBC where the coordinate system was originated. Severity of the crack was defined by $\beta=2e/h$, where $2e$ stands for the total reduction in depth due to the crack (e for each side). The entire structure was subject to a transverse mono-frequency excitation, $F_0\delta(x+d)e^{i\omega t}$, d (d=0.08 m) away from the origin, as indicated in Fig. 7.

The entire structure was modeled using Euler–Bernoulli beam finite elements, and the crack was simulated using a specific crack element with a reduced size in its depth compared with that of the intact region. Mode superposition method was recalled to solve the system equation. Let $\mathbf{W}_*^i(\omega_i)$ be the ith-order mode shape vector of the structure, and ω_i

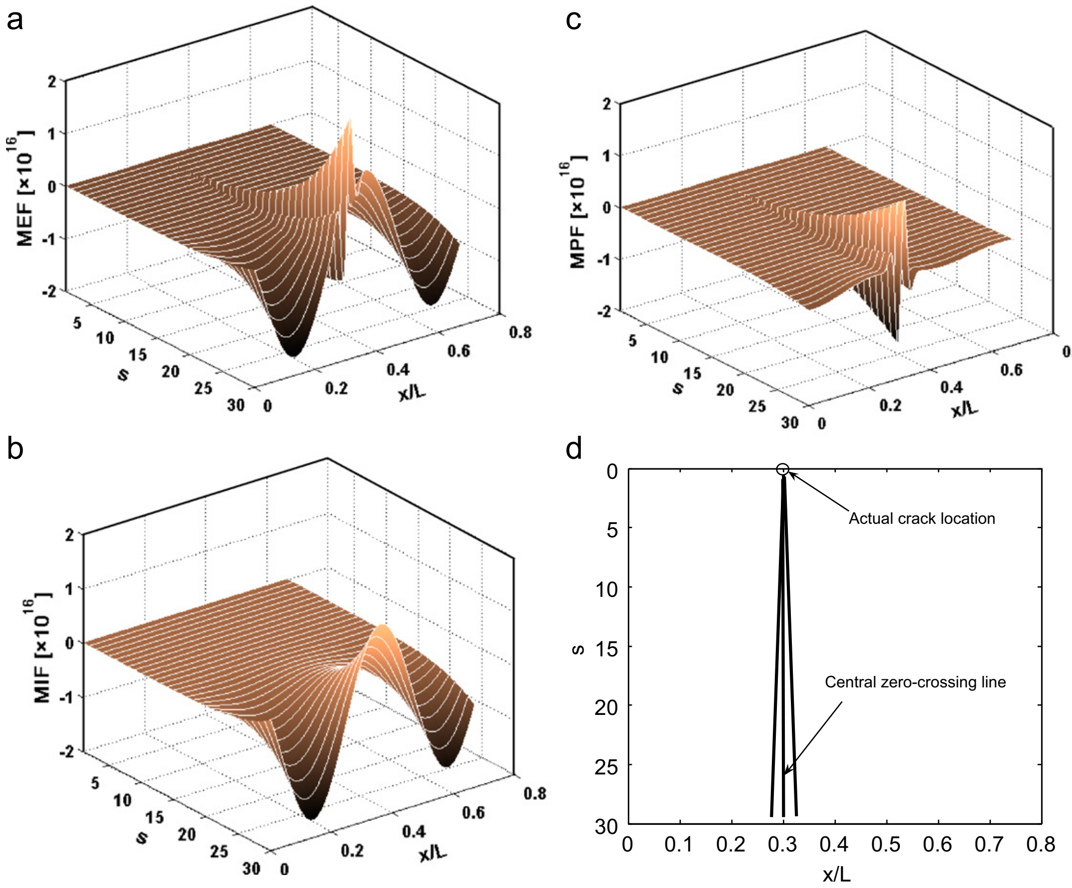

Fig. 6. Graphical representation of the multi-scale pseudo-force model for an EBC containing a crack (Damage Scenario II in Table 1): (a) *MEF* ($g^5(x)$); (b) *MIF* ($g^1(x)$); (c) *MPF*; (d) contour map of (c).

the corresponding modal frequencies. Then, the transverse displacement magnitude vector of the structure, $\mathbf{W}_*(\omega)$, can be expressed as [39]

$$\mathbf{W}_*(\omega)=\sum_i \frac{\mathbf{W}^i_*(\omega_i)[\mathbf{W}^i_*(\omega_i)\mathbf{F}]}{\omega_i^2-\omega^2}, \tag{30}$$

where $\mathbf{F}$ is the magnitude vector of excitation force applied to the structure, which is non-zero at and only at $x=-d$. From $\mathbf{W}_*(\omega)$ obtained by Eq. (30), the nodal transverse displacement vector, $\mathbf{W}(\omega)$, can further be extracted, and it corresponds to $W(x)$ in the enhanced model defined by Eq. (28), under the current excitation with a frequency of ω.

A series of damage scenarios was considered, as detailed in Table 1, by changing damage severity e in $\beta=2e/h$, *SNR* and frequency of the excitation, so as to examine the accuracy and effectiveness of the developed model in identifying damage of different severities under the influence of measurement noise. For reference, the modal frequencies of the structure, right before and after the excitation frequency, were also shown in the table. $\mathbf{W}(\omega)$ in all the damage scenarios were obtained using the same modeling technique aforementioned. By way of illustration, $\mathbf{W}(\omega)$ for Damage Scenarios III, V and VIII, as three typical examples, are shown in Fig. 8, from which direct awareness of any perturbance to $\mathbf{W}(\omega)$ due to existence of damage was vain.

5.2. Multi-scale filter for trend component of $\mathbf{W}(\omega)$

It is understandable that the damage of relatively small dimension such as a fine crack causes local perturbance to structural dynamic characteristics more phenomenally at higher frequencies. A captured $\mathbf{W}(\omega)$ manifests collective contributions from both a low-frequency trend component and a crack-induced local high-frequency perturbance. To stand out the local perturbance for damage identification, the trend component should ideally be filtered.

In most existing damage identification practices using CWT, the lower-order wavelets with less vanishing moments, compared to the order of $\mathbf{W}(\omega)$, are often selected. It is however envisaged that these lower-order wavelets may be insufficient to cancel the trend component of $\mathbf{W}(\omega)$. To benefit understanding, CWT-processed $\mathbf{W}(\omega)$ for Damage

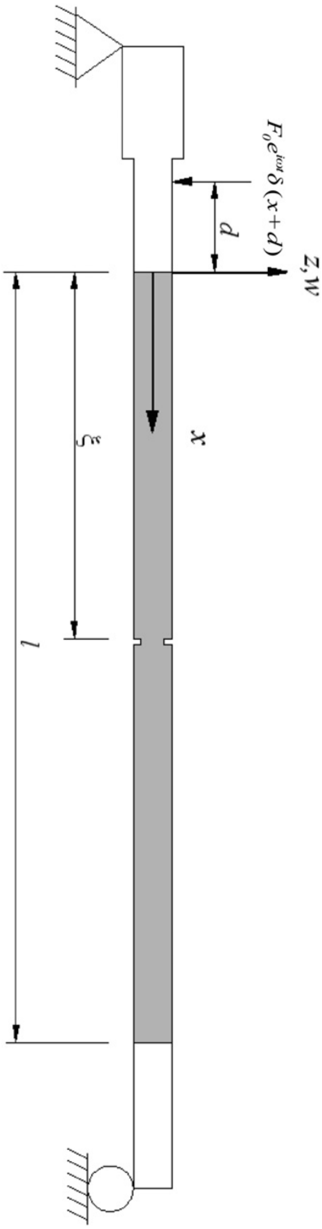

Fig. 7. Cracked EBC contained in a steel structural system for simulation.

Scenarios III–VIII is displayed in Fig. 9(a)–(f), respectively, as six representatives, in which a lower-order wavelet, the 5th-order Gaussian wavelet, $g^5(x)$, was used as the wavelet. It can be seen that the remaining trend component of $\mathbf{W}(\omega)$ masks the damage-induced perturbance seriously in all scenarios. That is because the approximate order of wavelet $g^5(x)$ is insufficient to screen the low-frequency trend component of $\mathbf{W}(\omega)$. In contrast, if a higher-order wavelet with greater vanishing moments used, the process suffices to screen the trend components of $\mathbf{W}(\omega)$, as observed in Fig. 10 for the same six damage scenarios in which $g^8(x)$ was used. However, it is relevant to note that the use of higher-order wavelets brings additional challenges. As observed in Fig. 10, the measurement noise components become highly severe, compared with those cases shown in Fig. 9 in which $g^5(x)$ was used; in some situations such as Damage Scenarios VI and VIII, the noise corrupts the crack-induced local singularity, making it impossible to locate the crack.

The above deficiencies can be circumvented using the enhanced model. That is because *MPF* in the enhanced model depicts the damage-incurred perturbance exclusively, without any contribution from the trend component of $\mathbf{W}(\omega)$; under such a circumstance lower-order wavelet ($g^5(x)$) suffices to pinpoint the damage precisely. In this sense, the model serves as a multi-scale filter to screen the trend component while simultaneously retaining the pseudo-force generated by the damage. To demonstrate such an advantage over conventional CWT analysis, Fig. 11 shows the results obtained using the

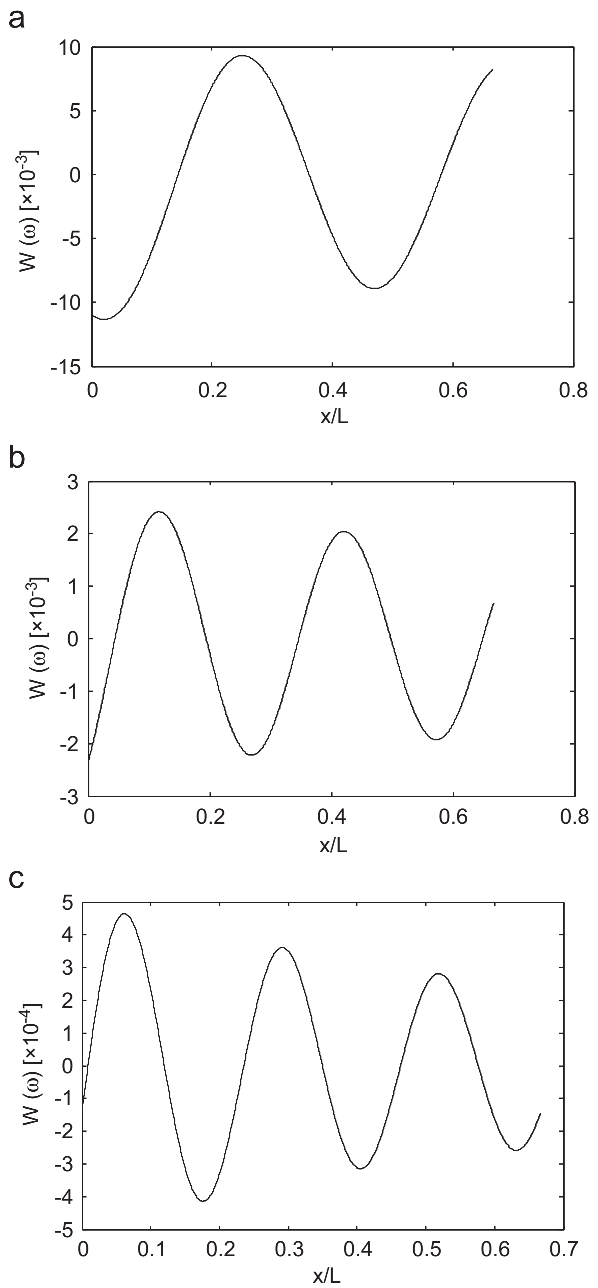

Fig. 8. $W(x)$ of the EBC in Fig. 7 under three representative damage scenarios: (a) III; (b) V; (c) VIII.

enhanced model for the six damage scenarios. The clear identification results accentuate the capability of the enhanced model in isolating perturbance associated with damage from the trend components of $\mathbf{W}(\omega)$.

5.3. *Multi-scale filter for random noise of* $\mathbf{W}(\omega)$

Apart from the abovementioned merit in filtering low-frequency trend component of $\mathbf{W}(\omega)$, the multi-scale pseudo-force model additionally presents advantages in removing random measurement noise in $\mathbf{W}(\omega)$. This property can be explained as follows. Recalling the property descried in Eq. (22), the convolution of $\mathbf{W}(\omega)$ with $\overline{g}_s^5(x)$ in *MEF* and the convolution of $\mathbf{W}(\omega)$ with $\overline{g}_s^1(x)$ in *MIF* in Eq. (28) can be expressed in a general form as

$$\mathbf{W}(\omega)*\overline{g}_s^n(x)(u)=\mathbf{W}(\omega)*C_n(-1)^n s^n\frac{\mathrm{d}^n\overline{g}_s^0(x)}{\mathrm{d}x^n}(u)=C_n(-1)^n s^n\frac{\mathrm{d}^n}{\mathrm{d}u^n}(\mathbf{W}(\omega)*\overline{g}_s^0(x))(u). \tag{31}$$

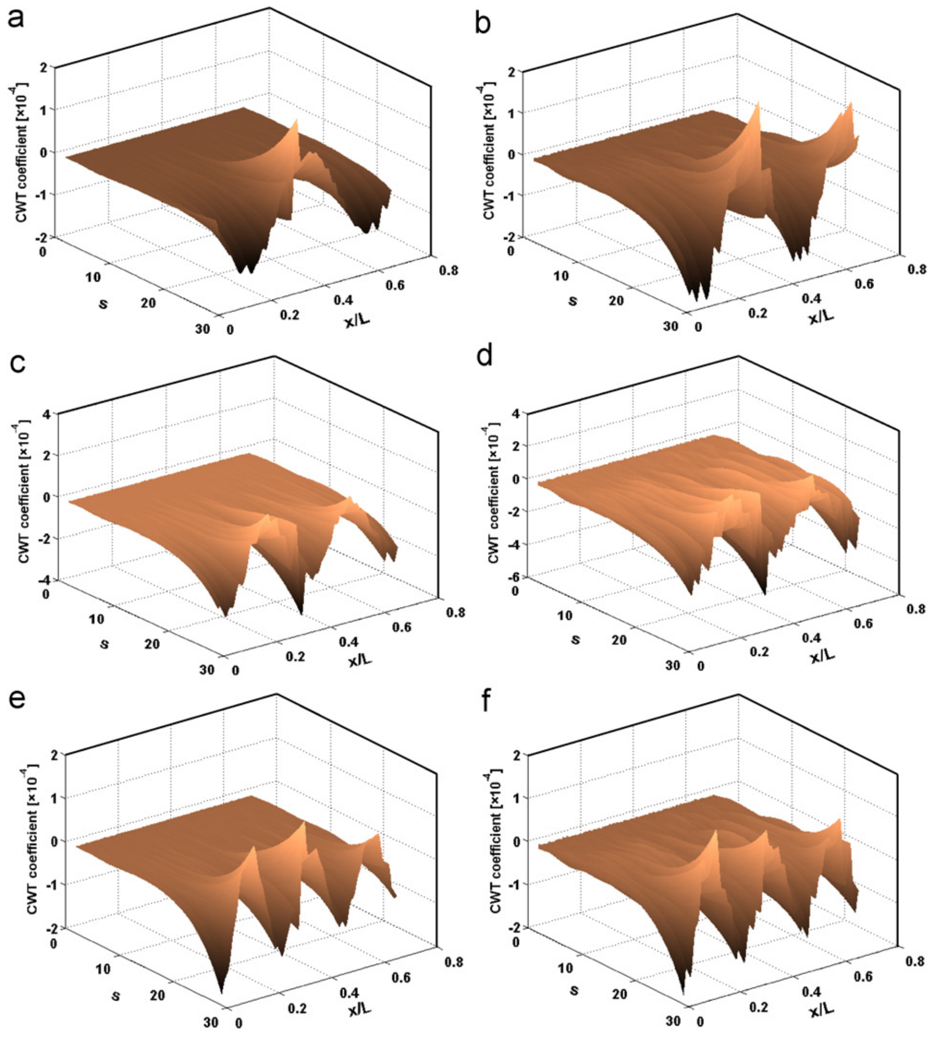

Fig. 9. CWT coefficients (using lower-order wavelet $g^5(x)$) of $W(x)$ of the EBC under six damage scenarios: (a) III; (b) IV; (c) V; (d) VI; (e) VII; (f) VIII.

Focusing on the rightmost-hand-side term, $\mathbf{W}(\omega)$ is first smoothed by $\bar{g}_s^0(x)$ through convolution and then differentiated with respect to space variable, u, for n times (n is an integer). Thus $\bar{g}_s^n(x)$ can be treated as a multi-scale smoothing-differential operator. The capacity of smoothing is able to filter random measurement noise while the property of differentiation facilitates to protrude the local perturbance caused by damage.

On the other hand, $\mathbf{W}(\omega)$ can be deemed as the combination of a substantial signal component, $\mathbf{W}_{\mathbf{singal}}(\omega)$, captured under noise-free conditions, and a random noise component, $\mathbf{W}_{\mathbf{noise}}(\omega)$. Described by the enhanced model, the amplitudes of absolute value of CWT coefficients of these two components ($|\mathcal{W}_{g^n}^{\mathrm{W}_{\text{signal}}}(s,u)|$ and $|\mathcal{W}_{g^n}^{\mathrm{W}_{\text{noise}}}(s,u)|$), obtained using Gaussian wavelet $g^n(x)$, exhibit different characteristics across scales. For $\mathbf{W}_{\mathbf{singal}}(\omega)$, it has

$$|\mathcal{W}_{g^n}^{\mathrm{W}_{\text{signal}}}(s,u)| \le A s^{a+1/2}, \tag{32}$$

where A is a constant, and a is the Lipschitz exponent [36]; while for $\mathbf{W}_{\mathbf{noise}}(\omega)$, one has

$$E(|\mathcal{W}_{g^n}^{\mathrm{W}_{\text{noise}}}(s,u)|^2) = \frac{\|g^n\|^2}{s}, \tag{33}$$

where function E denotes *mathematical expectation*. Eqs. (32) and (33) allude to that $|\mathcal{W}_{g^n}^{\mathrm{W}_{\text{signal}}}(s,u)|$ increases whereas $|\mathcal{W}_{g^n}^{\mathrm{W}_{\text{noise}}}(s,u)|$ decreases with the increase of scale, as explained by an example (Damage Scenario I) shown in Fig. 12. Thus, $\bar{g}_s^n(x)$ can serve as a joint multi-scale operator to suppress noise and meanwhile strengthen damage-induced singularity in $\mathbf{W}(\omega)$ gradually with the increase of scale.

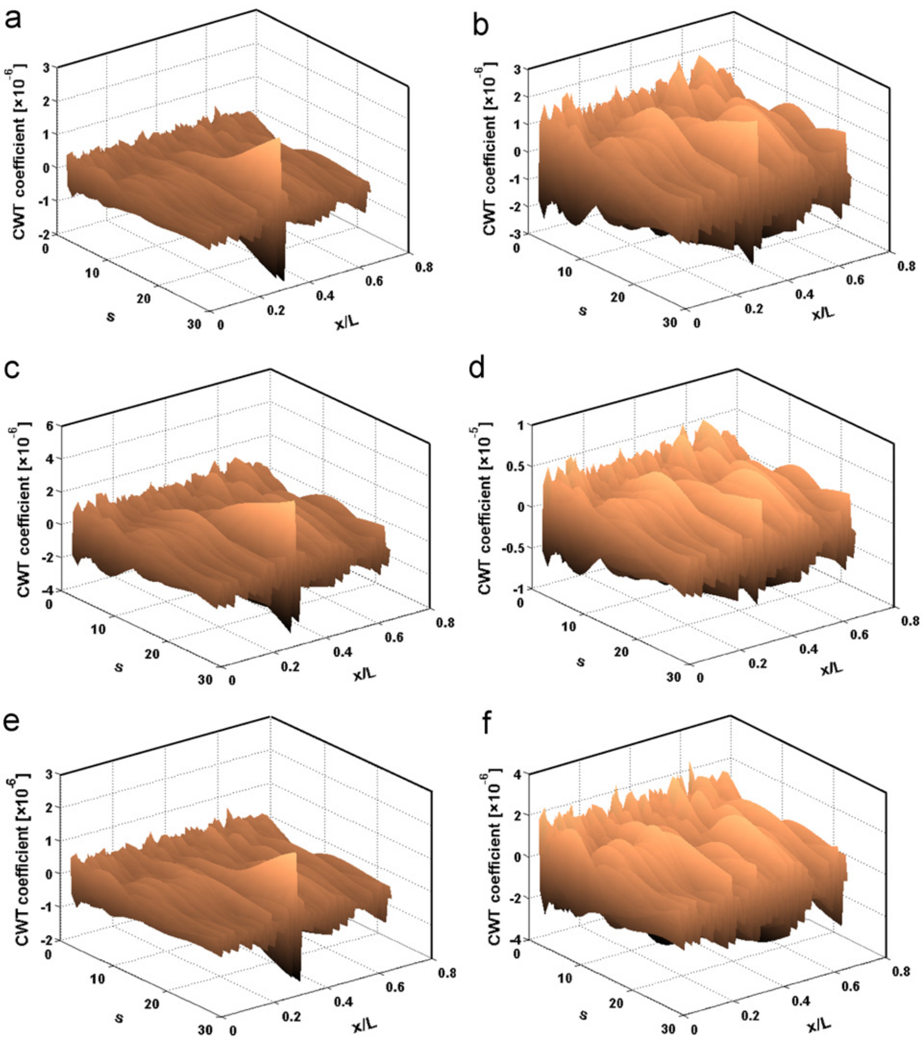

Fig. 10. CWT coefficients (using higher-order wavelet $g^8(x)$) of $W(x)$ of the EBC under six damage scenarios: (a) III; (b) IV; (c) V; (d) VI; (e) VII; (f) VIII.

Endowed with the capacities of multi-scale filtering for low-frequency trend component and high-frequency noise components in a captured $\mathbf{W}(\omega)$, respectively detailed in Sections 5.2 and 5.3, the enhanced pseudo-force model is inherently able to put crack-induced local perturbance prominence while at the same time tolerate various measurement noise and uncertainties.

6. Experimental validation

The proposed damage identification algorithm based on the enhanced multi-scale pseudo-force model was testified experimentally with the assistance of a scanning laser vibrometer (SLV). An aluminum structural system (aluminum 6061, $\rho_0 = 2700\ \mathrm{kg/m^3}$) containing an EBC was prepared. The structural system had one fixed end and one free end of irregular shape, as seen in Fig. 13, with all dimensions indicated in the figure. A through-width crack, measuring 1.2 mm long (along beam span) and 2 mm deep, was introduced to the EBC, 220 mm away from the clamped end. An out-of-plane mono-frequency excitation force at 2 kHz was applied along z-direction at a point 25 mm from the free end edge, using an electromechanical shaker (B&K 4809). The current selection of excitation frequency was based on a pre-spectrum analysis. In the EBC, out-of-plane velocities at all measurement points along the central line of the beam (evenly distributed with a spacing interval of 2.6 mm) were captured using an SLV (Polytecis® PSV-400). Note that the velocity was acquired from the intact surface of the beam, opposite to which lay the damage. The experiment set-up was photographed in Fig. 14. The captured velocities were mathematically integrated to achieve the out-of-plane displacement responses of the beam (i.e., $\mathbf{W}(\omega)$) using a FAST-SCAN function provided by the SLV system.

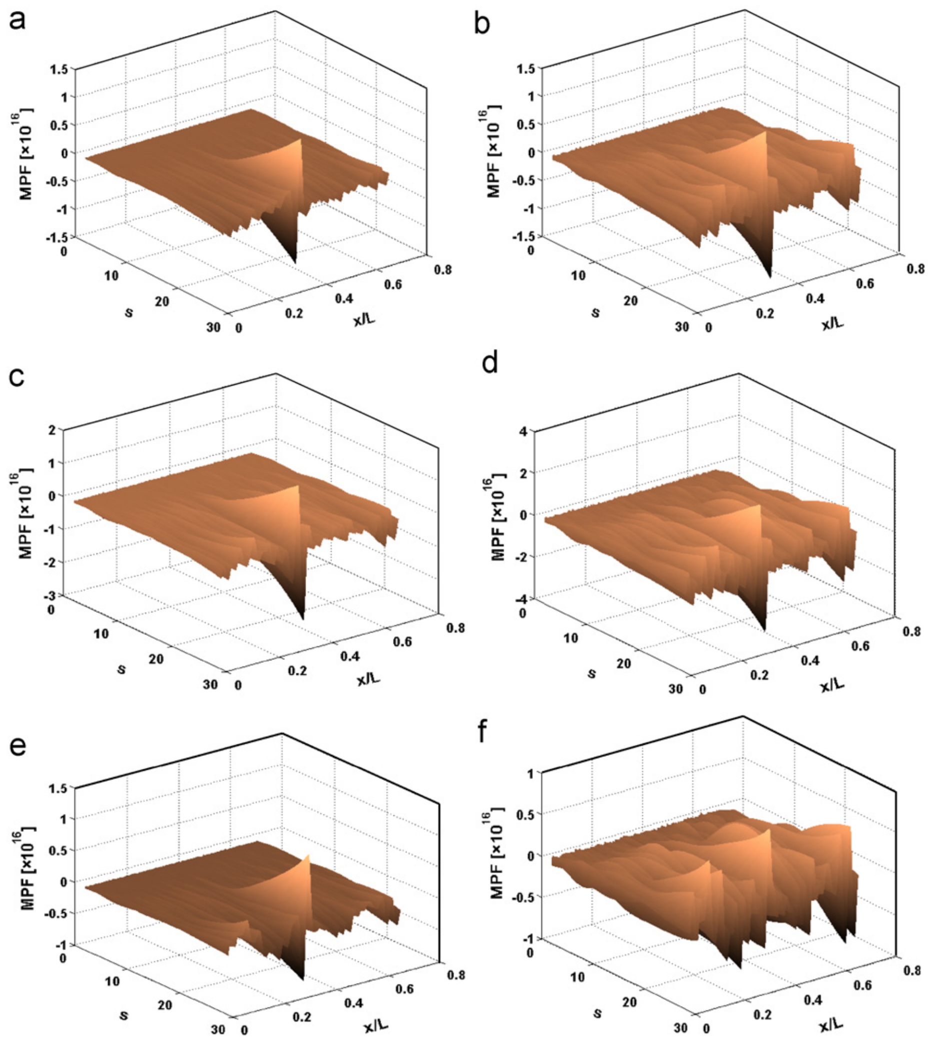

Fig. 11. *MPF* in the pseudo-force model for the EBC under six damage scenarios: (a) III; (b) IV; (c) V; (d) VI; (e) VII; (f) VIII.

6.1. Using traditional CWT-based analysis

For comparison, traditional CWT-based analysis was first applied to process $\mathbf{W}(\omega)$ for identifying the crack. The original $\mathbf{W}(\omega)$ and its corresponding CWT-processed results using $g^5(x)$ and $g^8(x)$ wavelets are displayed in Fig. 15(a)–(c), respectively. In original $\mathbf{W}(\omega)$, Fig. 15(a), characteristics associated with damage are imperceptible. In Fig. 15(b), owing to the fact that $g^5(x)$ has a lower approximate order compared to that of $\mathbf{W}(\omega)$, such a wavelet is unable to screen the low-frequency trend component of $\mathbf{W}(\omega)$ as explained in Section 5.2. The trend component overwhelms crack-induced perturbance largely, failing to indicate the presence of any damage. In Fig. 15(c), although $g^8(x)$ suffices to remove the trend component because it has a higher approximate order comparable with that of $\mathbf{W}(\omega)$, the high-frequency noise components in $\mathbf{W}(\omega)$ become pronounced after the transform, masking crack-induced perturbance as well. Neither of the two wavelets is able to deliver satisfactory identification results.

6.2. Using enhanced multi-scale pseudo-force model

Using the enhanced multi-scale pseudo-force model, the identification results are shown in Fig. 16. Fig. 16(a) and (b) shows terms *MEF* and *MIF* of the model, respectively. Due to the inherent capacities of the model in isolating low-frequency trend component and high-frequency measurement noise, *MPF* exhibits prominent changes only at the location where damage exists, as clearly observed in Fig. 16(c). Characterized by *MPF* ($MPF = -C_5 s^4 K g_s^1(u-\xi)$), in Eq. (28), the model presents the pattern of $-C_5 s^4 K$-scaled $g_s^1(u-\xi)$ in identification results, where damage location can be determined by finding the zero-crossing lines on $s-x$ plane at $u=\xi$.

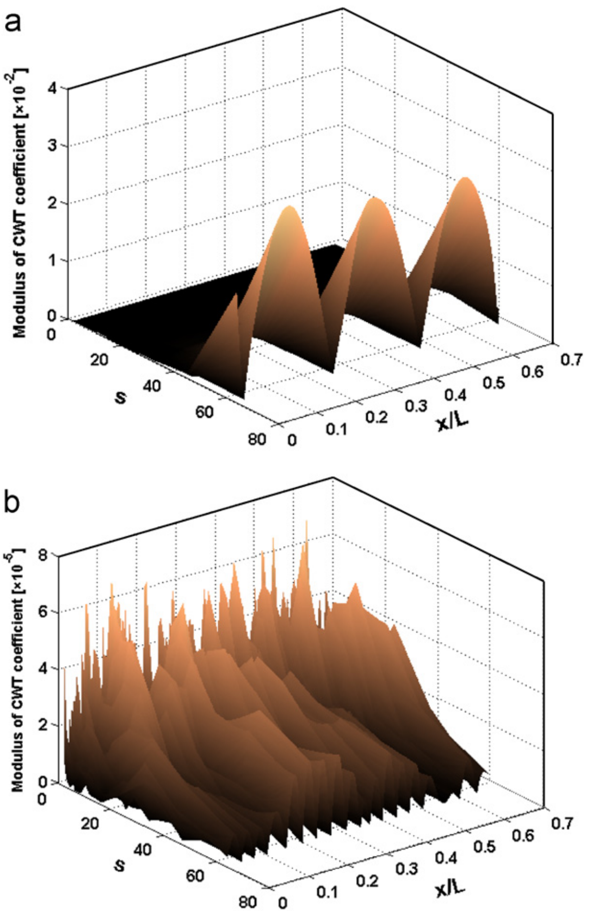

Fig. 12. Variations of CWT coefficient modulus of (a) $\mathbf{W}_{\text{singal}}(\omega)$ and (b) $\mathbf{W}_{\text{noise}}(\omega)$ (for Damage Scenario I).

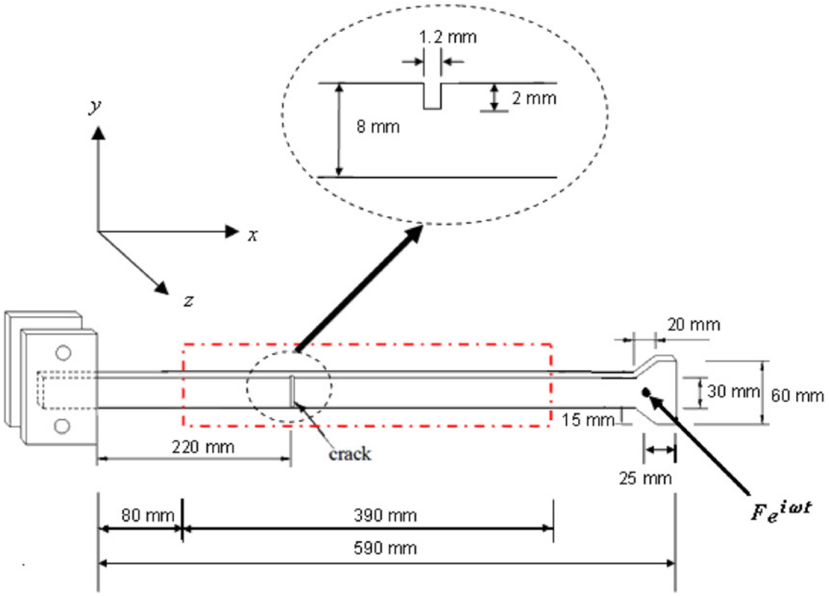

Fig. 13. A clamped-free structural system containing an EBC with a through-width crack for experimental validation.

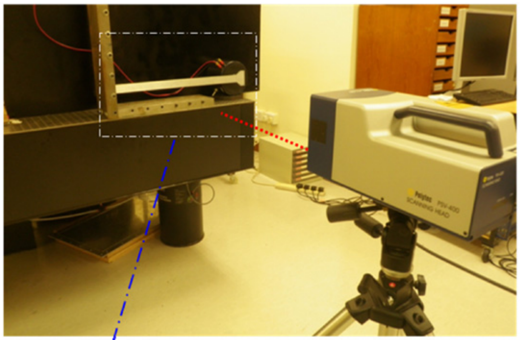

Experimental setup (damage was located on the surface opposite to the one from which the measurement was conducted)

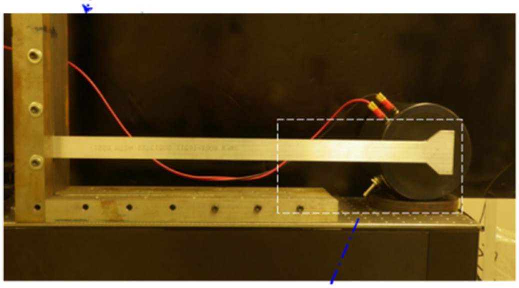

Zoomed-in part showing excitation using an electromechanical shaker

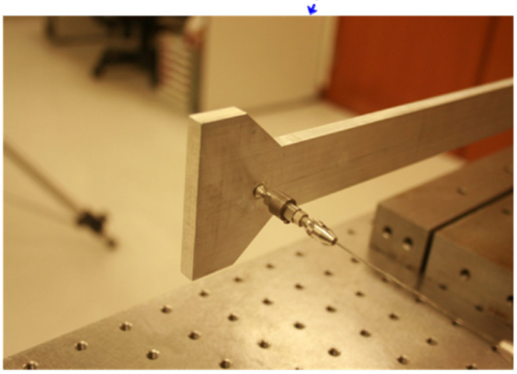

Zoomed-in part showing excitation point (viewed from back of the beam)

Fig. 14. Experimental setup for acquiring $W(x)$ using an SLV from the intact beam surface (i.e., the surface opposite to which lay the damage).

To further protrude characteristics of the damage, $\overline{g}_s^1(x)$ was employed to convolute the s-scale vector of *MPF* across the x axis, to generate a series of correlation coefficients at very single scale s, giving rise to Fig. 16(d). Each coefficient represents the degree of similarity between $\overline{g}_s^1(x)$ and local components of s-scale vector of *MPF* centered at x. The damage could be located more clearly when the correlation coefficient reached its maximum. In Fig. 16(d), the major ridges across the scale axis, comprising large correlation coefficients at every single scale, point out possible locations of the damage. On the other hand, it is noticed that, as scale increases, the damage-induced perturbance is strengthened progressively (i.e., better noise-tolerance), whereas at the expense of reduced degree of localization due to the wider supports of sub-wavelets (i.e., reduced accuracy). Allowing for this, damage locating should ideally be conducted at smaller scale, by tracking the major ridges of correlation coefficient surface in Fig. 16(d) from larger to smaller scales, so as to achieve the best localization. This can be conveniently accomplished by finding the peak values of contour lines of correlation coefficient surface on the s–x plane. At the smallest scale of 2 in the discussed scale range for this validation, the crack was located at 218 mm away from the clamped end, in good agreement with the real location of the damage (220 mm).

7. Conclusions

In spite of its popularity in a large variety of applications pertaining to vibration-based damage detection, wavelet transform has often been used as an effective tool for noise removal and signal feature extraction only, performed without

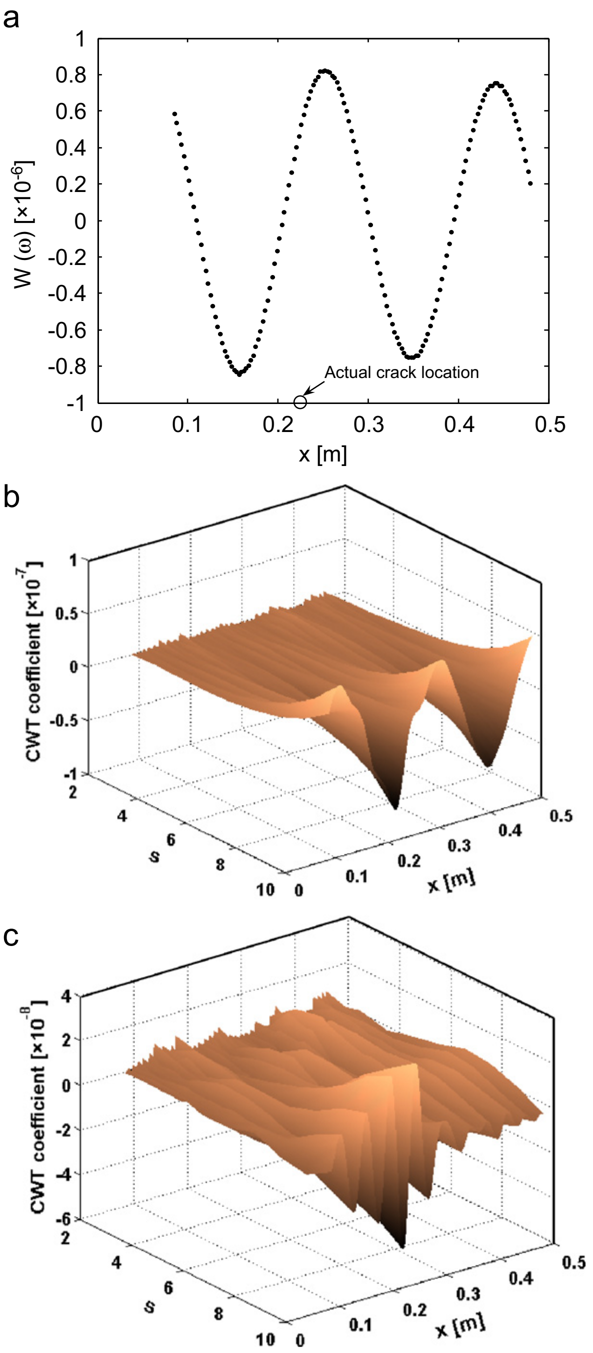

Fig. 15. Identification results obtained using conventional CWT-based analysis: (a) $W(x)$ experimentally captured; corresponding CWT coefficients obtained using (b) $g^5(x)$ and (c) $g^8(x)$.

concrete footstones of explicit mechanics models. The present study was dedicated to the development of a mechanics model for identification of structural damage and fine cracks in particular with explicit physical and mechanics implication, inherently addressing damage features. By quantifying damage-caused local perturbance to dynamic characteristics (higher-order differential equation of motion) of the structural component under inspection, a multi-scale pseudo-force model over wavelet domain was proposed. Residing on this mechanics model, a multi-scale damage identification algorithm was formulated, able to provide solutions to multi-scale modeling and identification of structural damage. The intrinsic combination between the wavelet transform and the mechanics model has endowed the detection algorithm with attractive features conducive to damage identification, including explicit revelation of damage characteristics, high sensitivity to fine damage of small dimensions, strong immunity to measurement noise and therefore enhanced

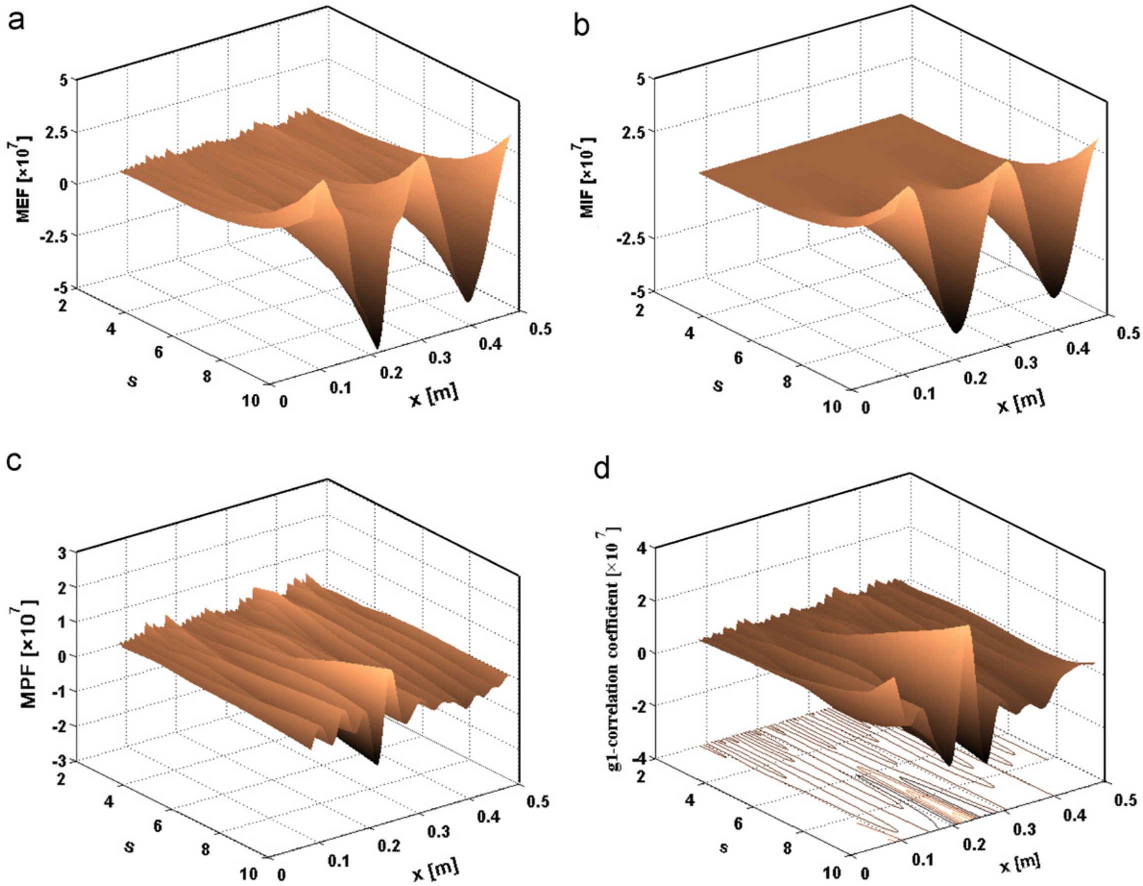

Fig. 16. Identification results obtained using enhanced model: (a) *MEF* ($g^5(x)$); (b) *MIF* ($g^1(x)$); (c) *MPF*; (d) correlation coefficients between $\overline{g}_s^1(x)$ and *MPF* (containing contour lines of correlation coefficient surface on s–x plane).

robustness in varying measurement environment and exemption of baseline data. The principle of the model was demonstrated using an Euler–Bernoulli beam component (EBC). As proof-of-concept validation, a fine crack in an EBC was identified with satisfactory precision using the model, in both numerical simulation and experiment. It is relevant to stress that the proposed methodology explores local dynamic equilibrium characteristics of a structural component irrespective of the complexity of the entire system beyond the inspection region. In that sense, the approach is potentially applicable to a complex structural system, provided that the dynamic characteristics of the individual structural components of interest can be locally described. It is also relevant to mention that lower-order derivatives of the captured dynamic response are currently under investigation to be integrated into the model, so as to achieve an optimal compromise between versatility of the model and desired identification accuracy, to be reported.

Acknowledgments

M. Cao is grateful to National Natural Science Foundation of China for research grants (Grant numbers: 50978084 and 11172091). L. Cheng and Z. Su wish to acknowledge the supports given to them by the Hong Kong Polytechnic University through research projects G-U859, A-PL08 and A-PE1F.

References

[1] Y.J. Yan, L. Cheng, Z.Y. Wu, L.H. Yam, Development in vibration-based structural damage detection technique, Mech. Syst. Signal Process. 21 (2007) 2198–2211.
[2] D.E. Adams, Health Monitoring of Structural Materials and Components: Methods with Applications, Wiley, New York, 2007.
[3] H. Sohn, C.R. Farrar, F.M. Hemez, D.D. Shunk, D.W. Stinemates, B.R. Nadler, A Review of Structural Health Monitoring Literature: 1996–2001, Los Alamos National Laboratory Report, LA-13976-MS, 2003.
[4] C. Boller, Ways and options for aircraft structural health management, Smart Mater. Struct. 10 (2001) 432–440.
[5] C.R. Farrar, K. Worden, An introduction to structural health monitoring, Philos. Trans. R. Soc. A 365 (2007) 303–315.

[6] G.Y. Xu, W.D. Zhu, B.H. Emory, Experimental and numerical investigation of structural damage detection using changes in natural frequencies, J. Vib. Acoust. 129 (2007) 686–700.
[7] J.T. Kim, Y.S. Ryu, H.M. Cho, N. Stubbs, Damage identification in beam-type structures: frequency-based methods *vs*. mode shape-based method, Eng. Struct. 25 (2003) 57–67.
[8] M.S. Cao, Y. Lin, L.M. Zhou, Z. Su, R.B. Bai, Sensitivity of fundamental mode shape and static deflection for damage identification in cantilever beams, Mech. Syst. Signal Process. 25 (2) (2011) 630–643.
[9] V. Giurgiutiu, C.A. Rogers, Recent advancements in the electro-mechanical (E/M) impedance method for structural health monitoring and NDE, Proc. SPIE 3329 (1998) 536–547.
[10] Z.K. Peng, Z.Q. Lang, S.A. Billings, Nonlinear parameter estimation for multi-degree-of-freedom nonlinear systems using nonlinear output frequency response functions, Mech. Syst. Signal Process. 22 (2008) 1582–1594.
[11] N.V. Ha, J.C. Golinval, Damage localization in linear-form structures based on sensitivity investigation for principal component analysis, J. Sound Vib. 21 (2010) 4550–4566.
[12] D. Montalvão, N.M.M. Maia, A.M.R. Ribeiro, A review of vibration based structural health monitoring with special emphasis on composite materials, Shock Vib. Dig. 38 (4) (2006) 295–324.
[13] R.O. Curadellia, J.D. Rierab, D. Ambrosinia, M.G. Amania, Damage detection by means of structural damping identification, Eng. Struct. 30 (12) (2008) 3497–3504.
[14] Z.R. Lu, S.S. Law, Differentiating different types of damage with response sensitivity in time domain, Mech. Syst. Signal Process. 24 (8) (2010) 2914–2928.
[15] Z. Su, L. Ye, Guided Lamb waves for identification of damage in composite structures: a review, J. Sound Vib. 295 (3–5) (2006) 753–780.
[16] Z. Wei, L.H. Yam, L. Cheng, Detection of internal delamination in multi-layer composites using wavelet packets combined with modal parameter analysis, Compos. Struct. 64 (2004) 377–387.
[17] J. Vieira, F.G. Baptista, D.J. Inman, Time-domain analysis of piezoelectric impedance-based structural health monitoring using multilevel wavelet decomposition, Mech. Syst. Signal Process. 25 (5) (2011) 1550–1558.
[18] M.M.R. Taha, A. Noureldin, J.L. Lucero, T.J. Baca, Wavelet transform for structural health monitoring: a compendium of uses and features, Struct. Health Monit. 5 (3) (2006) 267–295.
[19] B.H. Kim, T. Park, G.Z. Voyiadjis, Damage estimation on beam-like structures using the multiresolution analysis, Int. J. Solids Struct. 43 (2006) 4238–4257.
[20] D.E. Newland, Wavelet analysis of vibration, part I: theory, J. Vib. Acoust. 116 (1994) 409–416.
[21] A.N. Robertson, C.R. Farrar, H. Sohn, Singularity detection for structural health monitoring using holder exponents, Mech. Syst. Signal Process. 17 (2002) 1163–1184.
[22] I. Daubechies, The wavelet transform, time–frequency localization and signal analysis, IEEE Trans. Inf. Theory 36 (5) (1990) 961–1005.
[23] X. Jiang, S. Mahadevan, Wavelet spectrum analysis approach to model validation of dynamic systems, Mech. Syst. Signal Process. 25 (2) (2011) 575–590.
[24] Q. Wang, X. Deng, Damage detection with spatial wavelets, Int. J. Solids Structures 36 (1999) 3443–3468.
[25] S.C. Zhong, S.O. Oyadiji, Detection of cracks in simply-supported beams by continuous wavelet transform of reconstructed modal data, Comput. Struct. 89 (2011) 127–148.
[26] A. Gentile, A. Messina, On the continuous wavelet transforms applied to discrete vibrational data for detecting open cracks in damaged beams, Int. J. Solids Struct. 40 (2003) 295–315.
[27] J.C. Hong, Y.Y. Kim, H.C. Lee, Y.W. Lee, Damage detection using the Lipschitz exponent estimated by the wavelet transform: applications to vibration modes of a beam, Int. J. Solids and Struct. 39 (2002) 1803–1816.
[28] M.S. Cao, P.Z. Qiao, Integrated wavelet transform and its application to vibration mode shapes for the damage detection of beam-type structures, Smart Mater. Struct. 17 (2008) 055014 (17pp).
[29] E. Castro, M.T. Garcia-Hernandez, A. Gallego, Defect identification in rods subject to forced vibrations using the spatial wavelet transform, Appl. Acoust. 68 (2007) 699–715.
[30] A. Messina, Refinements of damage detection methods based on wavelet analysis of dynamical shapes, Int. J. Solids Struct. 45 (2008) 4068–4097.
[31] Z. Hou, M. Noori, R. Amand St., Wavelet based approach for structural damage detection, J. Eng. Mech. 126 (7) (2000) 677–683.
[32] C.-C. Chang, L.-W. Chen, Detection of the location and size of cracks in the multiple cracked beam by spatial wavelet based approach, Mech. Syst. Signal Process. 19 (1) (2005) 139–155.
[33] F.-K. Chang, Introduction to health monitoring: context, problems, solutions, presentation, in: Proceedings of the First European Pre-Workshop on Structural Health Monitoring, Paris, France, 2002.
[34] P.F. Rizos, N. Aspragathos, A.D. Dimarogonas, Identification of crack location and magnitude in a cantilever beam from the vibration modes, J. Sound Vib. 138 (3) (1993) 381–388.
[35] S. Timoshenko Jr., D.H. Young, W. Weaver, Vibration Problems in Engineering, fourth ed., Wiley, New York, 1974.
[36] S. Mallat, A Wavelet Tour of Signal Processing, third ed., Academic Press, San Diego, 2008.
[37] E. Sazonov, P. Klinkhachorn, Optimal spatial sampling interval for damage detection by curvature or strain energy mode shapes, J. Sound Vib. 285 (4–5) (2005) 783–801.
[38] M. Rucka, Damage detection in beams using wavelet transform on higher vibration modes, J. Theor. Appl. Mech. 49 (2) (2011) 399–417.
[39] D.J. Inman, Engineering Vibration, second ed., Prentice Hall, Upper Saddle River, 2000.